The variable continuous bimaterial interface in the San Jacinto fault zone (SJFZ) revealed by dense seismic array analysis of fault zone head waves

Pieter-Ewald Share[1], Frank L. Vernon[2] and Yehuda Ben-Zion[3]

1. College of Earth, Ocean, and Atmospheric Sciences, Oregon State University, Corvallis, OR Email: **pieter.share@oregonstate.edu**
2. Institute of Geophysics and Planetary Physics, Scripps Institution of Oceanography, La Jolla, CA
3. Department of Earth Sciences and Southern California Earthquake Center, University of Southern California, Los Angeles, CA

Many large earthquake faults are complex and non-planar

- Ridgecrest, Kaikoura and El-Mayor Cucapah (Fig. 1) are all exemplary cases of recent multi-fault earthquake ruptures with complex kinematics and geometries.
- In these cases, damage is usually distributed and seismicity patterns can be broad[1,2] and diffuse (Fig. 1).
- Quantifying these complexities is key for advances in rupture physics[3,4] and understanding radiated energy[5,6].
- New tools are required to better inform the structural properties of complex earthquake prone faults and nullify the need for common simplifying assumptions.

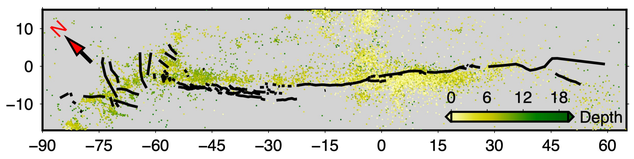

Figure 1: *The complex El-Mayor Cucapah rupture[7] and all relocated post-2010 seismicity[8].*

Large faults are often bimaterial

- In many instances[9,10,11], large offset faults juxtapose two crustal blocks of different material properties.
- Faults initiating along existing boundaries do the same.
- These **bimaterial faults** generate critically refracted **fault zone head waves (FZHW)** that can be used to pinpoint complex bimaterial fault locations at depth and reveal the variable velocity contrasts across them.

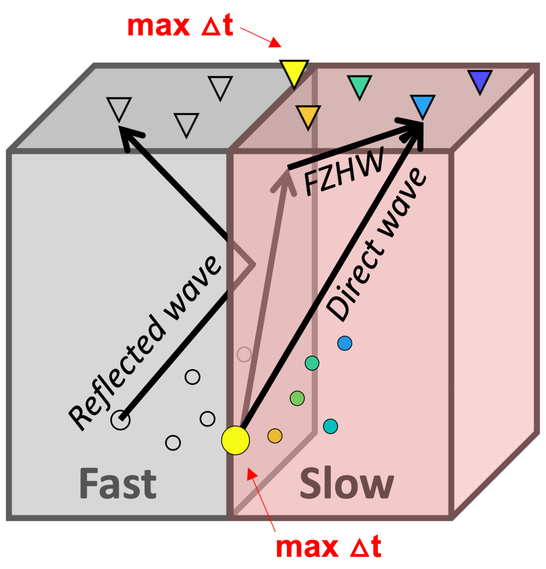

A novel method to illuminate deep complex bimaterial faults

1. Identify[12,13,14] and confirm[15,16] FZHWs preferably first in large-N array data that cross target fault zones.
2. Use confirmed events as templates for FZHW detection in other spatiotemporally correlated events and arrays along the same fault.
3. Quantify differential times (Δt) for all events and arrays.
4. Find Δt maxima (fault locations) for different across-fault transects.
5. Calculate velocity contrasts from neighboring on-fault event Δt.

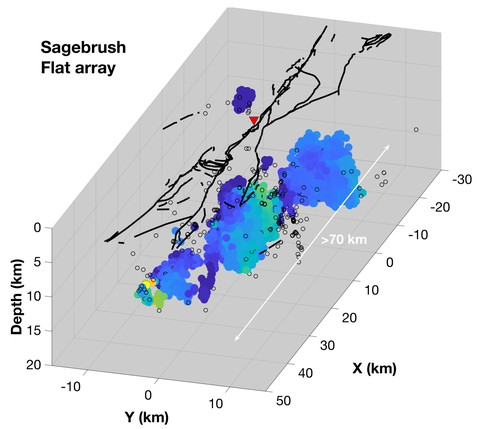

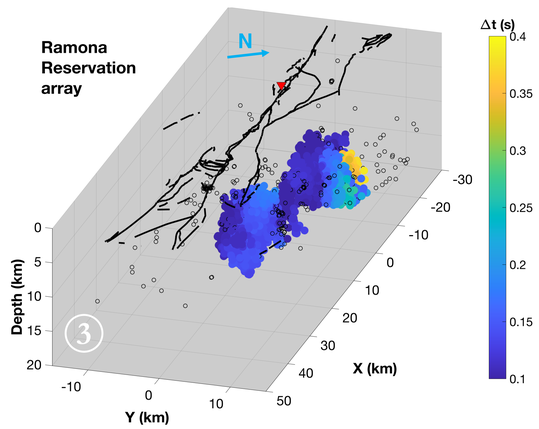

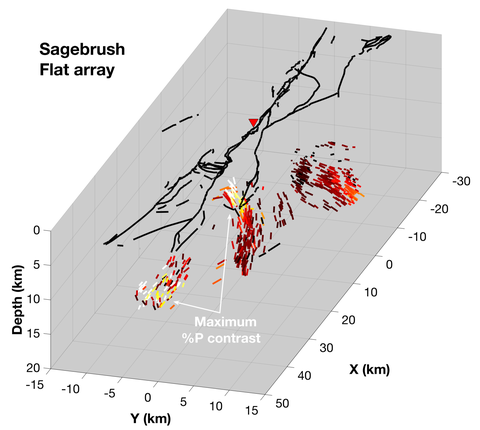

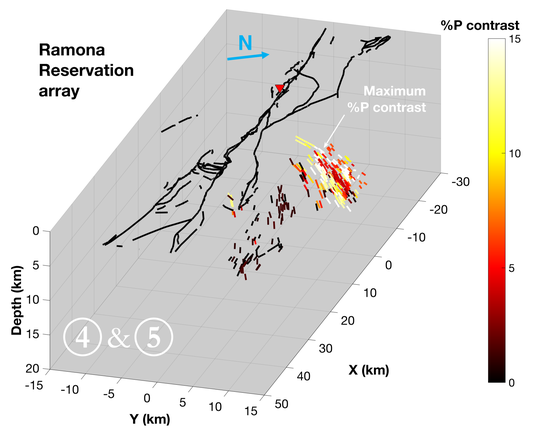

Figure 2 (Left): *Basic features of fault zone head waves (FZHWs) and other key seismic phases around a bimaterial fault with stations (triangles) and local earthquakes (circles) scattered across the fault. The colors of the symbols depict differential times (Δt) between FZHWs and trailing direct waves (yellow = large & blue = small). In this scenario, the station with maximum Δt pinpoints the fault location at the surface and the event with maximum Δt does the same at depth. A FZHW propagating from this event to that surface station illuminates a continuous bimaterial fault segment between the two.*

Figure 5 (Above): *Bimaterial fault segments and associated P-wave velocity contrasts identified for the deep SJFZ using on-fault event Δt values. Colors denote %P contrast and orientation, the direction in which this contrast exists. These short line segments illuminate the location/geometry of the primary bimaterial SJFZ at depth. Note how the estimated contrasts change from the Sagebrush Flat (left) to Ramona sites (right). This may suggest the observed contrasts are a function of direction, i.e.,* ***velocity contrast anisotropy****.*

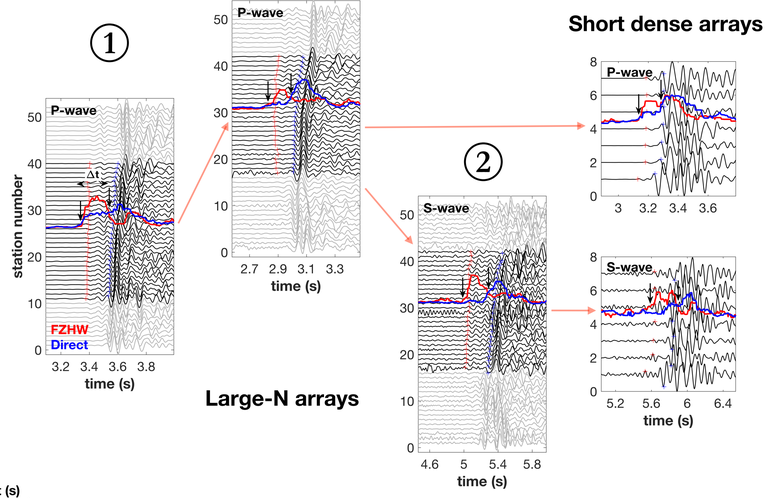

Figure 3 (Above): *The cascading manner in which P FZHWs are first detected and confirmed in large-N arrays, and then those detections and events are used as templates to detect S FZHW in the same arrays and P and S FZHWs in collocated dense arrays and for other events. The differential time (Δt) per event and array between FZHW (red) and direct wave (blue) arrivals is calculated using phase-weighted stack[17] (red and blue profiles) and energy[18] differences between the two. These examples are for waveforms recorded by arrays at the Sagebrush Flat site (see Fig. 4 left).*

Figure 4 (Left): *Differential times (Δt) calculated as in Fig. 3 for all FZHW generating events recorded at the Sagebrush Flat (left) and Ramona Reservation (right) sites. >14,000 events are confirmed using >1,000 large-N and dense array stations. Both sites are located along the San Jacinto fault zone (SJFZ) but about 10 km apart (red triangles). Empty black circles denote reference events that do not generate FZHWs but also locate near the bimaterial SJFZ at depth (slightly on the fast velocity side).*

Results for the complex SJFZ

- >14,000 FZHW generating events identified with >1,000 large-N and dense seismic array stations.
- Estimated contrast for the SJFZ is variable along-strike and in depth: 0 to >15% for P and an average of 2% for S (not shown).
- Estimated contrast is also a function of array location, implying velocity contrast anisotropy.
- Clear northeast dipping bimaterial segments at depth, e.g., northwestern SJFZ.
- Total length of the bimaterial interface (>70 km) is larger than the total SJFZ dextral offset (25 km), suggesting it initiated along an existing boundary.
- All these features have important implications for rupture physics along the SJFZ and other faults.

1. Powers, P. M., & Jordan, T. H. (2010). Distribution of seismicity across strike-slip faults in California. Journal of Geophysical Research: Solid Earth, 115(B5).
2. Perrin, C., Waldhauser, F., & Scholz, C. H. (2021). The Shear Deformation Zone and the Smoothing of Faults With Displacement. Journal of Geophysical Research: Solid Earth, 126(5), e2020JB020447.
3. Idini, B., & Ampuero, J.-P. (2020). Fault-Zone Damage Promotes Pulse-Like Rupture and Back-Propagating Fronts via Quasi-Static Effects. Geophysical Research Letters, 47(23), e2020GL090736.
4. Sibona, H., Kammer, D. S., Adda-Bedia, M., & Fineberg, J. (2020). The onset of the frictional motion of dissimilar materials. Proceedings of the National Academy of Sciences, 117(24), 13379 LP – 13385.
5. Dunham, E. M., Belanger, D., Cong, L., & Kozdon, J. E. (2011). Earthquake Ruptures with Strongly Rate-Weakening Friction and Off-Fault Plasticity, Part 2: Nonplanar Faults. Bulletin of the Seismological Society of America, 101(5), 2308–2322.
6. Graves, R., & Pitarka, A. (2016). Kinematic Ground-Motion Simulations on Rough Faults Including Effects of 3D Stochastic Velocity Perturbations. Bulletin of the Seismological Society of America, 106(5), 2136–2153.
7. Fletcher, J. M., Teran, O. J., Rockwell, T. K., Oskin, M. E., Hudnut, K. W., Mueller, K. J., … González-García, J. (2014). Assembly of a large earthquake from a complex fault system: Surface rupture kinematics of the 4 April 2010 El Mayor–Cucapah (Mexico) Mw 7.2 earthquake. Geosphere, 10(4), 797–827.
8. Share, P.-E., Castro, R. R., Vidal-Villegas, J. A., Mendoza, L., & Ben-Zion, Y. (2021). High-resolution seismic imaging of the plate boundary in northern Baja California and southern California using double-pair double-difference tomography. Earth and Planetary Science Letters, 568, 117004.
9. Sutherland, R., Davey, F., & Beavan, J. (2000). Plate boundary deformation in South Island, New Zealand, is related to inherited lithospheric structure. Earth and Planetary Science Letters, 177(3), 141–151.
10. Le Pichon, X., Kreemer, C., & Chamot-Rooke, N. (2005). Asymmetry in elastic properties and the evolution of large continental strike-slip faults. Journal of Geophysical Research: Solid Earth, 110(B3).
11. Bennington, N. L., Thurber, C., Peng, Z., Zhang, H., & Zhao, P. (2013). Incorporating fault zone head wave and direct wave secondary arrival times into seismic tomography: Application at Parkfield, California. Journal of Geophysical Research: Solid Earth, 118(3), 1008–1014.
12. McGuire, J., & Ben-Zion, Y. (2005). High-resolution imaging of the Bear Valley section of the San Andreas fault at seismogenic depths with fault-zone head waves and relocated seismicity. Geophysical Journal International, 163(1), 152–164.
13. Li, Z., & Peng, Z. (2016). Automatic identification of fault zone head waves and direct P waves and its application in the Parkfield section of the San Andreas Fault, California. Geophysical Journal International, 205(3), 1326–1341.
14. Ross, Z. E., & Ben-Zion, Y. (2014). Automatic picking of direct P, S seismic phases and fault zone head waves. Geophysical Journal International, 199(1), 368–381.
15. Share, P.-E., Allam, A. A., Ben-Zion, Y., Lin, F.-C. & Vernon, F. L. (2019). Structural properties of the San Jacinto fault zone at Blackburn Saddle from seismic data of a dense linear array, Pure and Applied Geophysics, 176(3), 1169-1191.
16. Qin, L., Share, P.-E., Qiu, H., Allam, A. A., Vernon, F. L., & Ben-Zion, Y. (2021). Internal structure of the San Jacinto fault zone at the Ramona Reservation, north of Anza, California, from dense array seismic data. Geophysical Journal International, 224(2), 1225–1241.
17. Schimmel, M., & Paulssen, H. (1997). Noise reduction and detection of weak, coherent signals through phase-weighted stacks. Geophysical Journal International, 130(2), 497–505.
18. Jurkevics, A. (1988). Polarization Analysis of Three-component Array Data, Bull. Seism. Soc. Am., 78 (5), 1725-1743.